Revealing complex spin states in $GdNiAl_4Ge_2$

Keke Feng,[1,2] Jorge R. Galeano Cabral,[3,1] Kaya Wei,[1] and Ryan Baumbach[1,2]
[1]National High Magnetic Field Laboratory, Tallahassee, Florida, USA
[2]Department of Physics, Florida State University, Tallahassee, Florida, USA
[3]FAMU-FSU College of Engineering, Florida State University, Tallahassee, Florida, USA

(Received 20 May 2023; accepted 21 November 2023; published 19 December 2023)

There is ongoing interest in strongly correlated spin systems where the interplay between structural, charge, and spin degrees of freedom produces novel phenomena, including helical spin order, topologically protected spin textures (e.g., skyrmions), unconventional electronic band physics (e.g., flat bands), and other emergent states. Here we report results for $GdNiAl_4Ge_2$, which crystallizes in a rhombohedral structure that features geometrically frustrated triangular nets of lanthanide ions. Magnetic, thermodynamic, and electrical transport measurements reveal metallic behavior with antiferromagnetic-like ordering in small magnetic fields, which strongly evolves to produce a spin-flop transition and hysteresis for magnetic fields applied in the *ab* plane. This results in a region of the temperature-field phase space where the magnetic susceptibility of the field-cooled curves is smaller than that of the zero-field-cooled curves and where the ac magnetic response exhibits frequency- and field-dependent peaks only in the zero-field-cooled curves. This suggests the formation of history-dependent spin structures or domains with complex spin relaxation dynamics, possibly resembling what is seen in other materials with nontrivial spin textures. This establishes $GdNiAl_4Ge_2$ as a host for intriguing spin states and further focuses attention on this family of materials.

DOI: 10.1103/PhysRevMaterials.7.124409

I. INTRODUCTION

The materials $LnAuAl_4Ge_2$ (Ln = lanthanide) have attracted growing interest because they exhibit (i) rich temperature–magnetic-field ($T-H$) phase diagrams with multiple magnetically ordered states, some of which may relate to their geometrically frustrated triangular nets of Ln ions [1–5]; (ii) linear magnetoresistances at low temperatures that persist in the presence of different Ln ions [2,4]; and (iii) evidence for multiple surface states with nontrivial band topologies [6]. Several conventional trends are also observed, including that the ordering temperatures follow de Gennes scaling [4]. Taken together, these features establish this family of materials as a chemically tunable reservoir for novel phenomena and connects them to broader classes of complex magnetic metals including those with geometric frustration [7–11], topological protection [12–15], unconventional Hall effects [16,17], helical order [18], or skyrmion states [15,19–24].

Amongst these materials, those that include Gd are particularly useful as prototypes because of their half-filled $4f$ shell ($S = 7/2$, $L = 0$, and $J = 7/2$), which leads to limited crystal electric field effects and a localized spin-only magnetic moment. This creates the opportunity to identify phenomena that are associated with the interplay between spins, Fermi surface topography, and geometric frustration, in the absence of orbital effects. This motivated our previous studies of $GdAuAl_4Ge_2$, which revealed a complex $T-H$ phase diagram with multiple metamagnetic transitions for magnetic fields applied in the *ab* plane (i.e., in the triangular net plane) [1,2]. Magnetoresistance measurements also revealed anomalous linear magnetoresistance behavior within the ordered state for $H \parallel c$. More recently, angle-resolved photoemission spectroscopy (ARPES) measurements uncovered possible $\mathbb{Z}_2$ topology for some of the electronic bands [6]. Collectively, these results raise the possibility for a novel interplay between topology, magnetic frustration, and the magnetic ordering, highlighting the potential for novel behaviors to emerge in this family.

Here we extend our studies to $GdNiAl_4Ge_2$, which features the same centrosymmetric structure as the Au analog [5]. The replacement of $5d$ Au ions with $3d$ Ni ions is expected to lead to a lattice contraction, variation in the Fermi surface and thus the Ruderman-Kittel-Kasuya-Yosida (RKKY) interaction, and a weakened spin-orbit coupling, all of which will impact the electronic and magnetic states. Magnetic, thermodynamic, and electrical transport measurements uncover metallic behavior, with a bulk second-order phase transition at $T_{N1} = 20.4$ K. For magnetic fields $H \parallel c$, the feature at T_{N1} retains its antiferromagnetic character and is gradually suppressed with increasing H. Substantially more complex behavior is seen for $H \perp c$, where antiferromagnetic-like behavior occurs for small fields and a spin-flop transition with accompanying hysteresis [25–27] is seen for $\mu_0 H =$ 0.5–0.85 T. Over this field range the magnetic susceptibility of the field-cooled curves for $T < T_{N1}$ is smaller than that of the zero-field-cooled curves, suggesting the formation of history-dependent spin structures or domains. The ac magnetic susceptibility also exhibits frequency- and field-dependent peaks [both $\chi'(T)$ and $\chi''(T)$], indicating that there are complex spin relaxation dynamics in the spin-flop region. For fields above the hysteresis region, the antiferromagnetic order is gradually suppressed and collapses towards $T = 0$ K near 7 T.

These results reveal a complex phase diagram where magnetic frustration may play an important role. As a result, $GdNiAl_4Ge_2$ emerges as an intriguing spin system, with possible connections to other examples; e.g., those with skyrmion or other textured spin lattices such as Gd_2PdSi_3 [15], $Gd_3Ru_4Al_{12}$ [23], $GdRu_2Si_2$ [24], MnSi [28–31], FeGe [32–34], Cu_2OSeO_3 [35,36], $Fe_{1-x}Co_xSi$ [37,38], and $Fe_{5-x}GeTe_2$ [39]; or with unconventional domain patterns such as UMn_2Ge_2 [40] and $CeRu_2Ga_2B$ [41]. Given the diverse array of tunable spin states in the broader $LnTAl_4Ge_2$ (Ln = lanthanide and T = transition metal) family, this result draws further attention to this structure as an environment to search for strongly correlated magnetism and possibly even a metallic quantum spin liquid behavior [42].

II. EXPERIMENTAL METHODS

$GdNiAl_4Ge_2$ single crystals were grown using an aluminum molten metal flux method. Elements with purities >99.9% were combined in the molar ratio 1 (Gd) : 1 (Ni) : 15 (Al) : 5 (Ge) and loaded into 2-mL alumina Canfield crucibles [43]. The crucibles were sealed under vacuum in quartz tubes, heated to 800 °C at a rate of 48 °C/h, kept at 800 °C for 4 days, and then cooled to 700 °C at a rate of 6.25 °C/h. Excess flux was removed by centrifuging the tubes at 700 °C, after which single-crystal platelets were collected. $LuNiAl_4Ge_2$ single crystals were prepared following the same method.

Room temperature powder x-ray diffraction (PXRD) measurements were performed using a Rigaku SmartLab SE x-ray diffractometer with a Cu Kα source. The Rietveld refinement analysis was performed using WINPREP to assess the purity and determine the structure parameters. The principal c axis was identified by measuring the diffraction pattern on a polished flat crystal using the same system. As shown in Fig. 1, the data are described by a rhombohedral structure with the space group $R\bar{3}m$ (No. 166). Fits to the data yield lattice parameters and unit cell volumes $a = 4.0986(1)$ Å, $c = 30.9783(7)$ Å, and $V = 450.67(4)$ Å and $a = 4.0643(1)$ Å, $c = 30.6202(4)$ Å, and $V = 437.77(8)$ Å for the Gd and Lu analogs, respectively. Similar results were reported in the literature [5]. Figure 1(c) also shows the x-ray diffraction (XRD) patterns for a c-axis-aligned $GdNiAl_4Ge_2$ crystal, where only the (00l) diffraction peaks appear, indicating that the crystal surface is parallel to the ab plane. The powder XRD pattern for $LuNiAl_4Ge_2$ is shown in Fig. S1 of the Supplemental Material [44].

Isothermal dc magnetization $M(H)$ and magnetic susceptibility $\chi_{dc}(T)$ measurements were carried out for temperatures $T = 1.8$–300 K under applied magnetic fields of $\mu_0 H \leqslant 7$ T applied parallel (‖) and perpendicular (⊥) to the crystallographic c axis using a Quantum Design Magnetic Property Measurement System, MPMS3. The ac magnetic susceptibility $\chi'_{ac}(T)$ measurements were also performed using an oscillating field $\mu_0 H = 1$ mT at frequencies between 1 and 500 Hz and under applied dc magnetic fields $\mu_0 H \leqslant 1$ T using the same system. Specific heat C measurements were performed for $T = 1.8$–70 K in a Quantum Design Physical Property Measurement System using a conventional thermal relaxation technique. Electrical resistivity $\rho(T, H)$ measurements for temperatures $T = 1.8$–300 K and $\mu_0 H \leqslant 9$ T were performed in a four-wire configuration for polished single crystal using the same system. All measurements were performed on crystals similar to the one shown in the Fig. 1(b) inset.

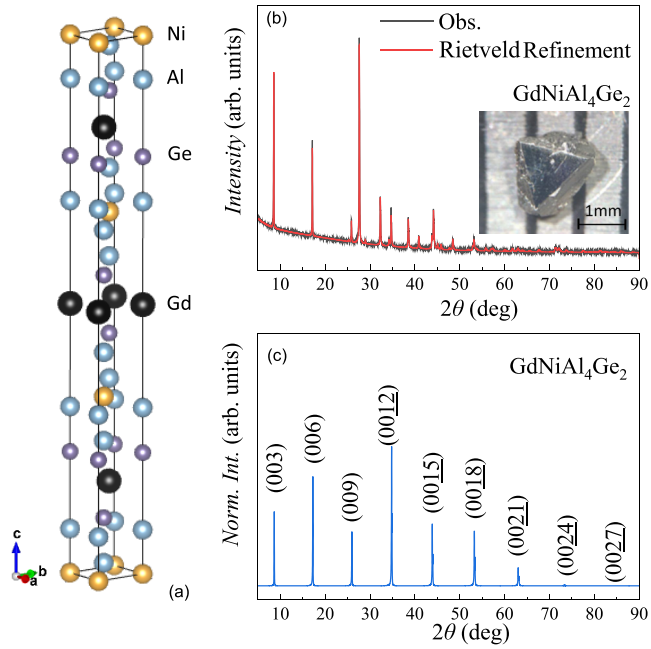

FIG. 1. (a) Crystal structure of $GdNiAl_4Ge_2$ [45]. (b) Rietveld refinements of powder x-ray diffraction patterns of $GdNiAl_4Ge_2$. The black curve is the observed experimental pattern, and the red curve is a pattern fit to the data used to determine lattice parameters. The inset shows a typical single-crystal specimen. (c) Powder x-ray diffraction data of a c-axis-aligned $GdNiAl_4Ge_2$ crystal. Norm. int., normalized intensity.

III. RESULTS

A. The dc magnetic properties

Figure 2 shows the temperature-dependent dc magnetic susceptibility $\chi_{dc}(T)$ for $GdNiAl_4Ge_2$ with magnetic fields $\mu_0 H = 0.5$ T applied parallel (‖) and perpendicular (⊥) to the crystalline c axis. As shown in Fig. 2(b), the inverse magnetic susceptibility $\chi_{dc}^{-1}(T)$ is linear for $T = 30$–300 K, revealing Curie-Weiss behavior described by the expression $\chi = C/(T - \theta)$. Fits to the data for $H \perp c$ yield the parameters $\theta = 7.4$ K and $2.82\sqrt{C} = \mu_{eff} = 7.93$ μ_B/Gd atom, where the positive θ indicates a ferromagnetic spin exchange and the effective magnetic moment μ_{eff} is consistent with the value for trivalent gadolinium ($\mu_{eff} = 7.94$ μ_B/Gd atom [46]). This implies that the Ni d electrons do not carry a net magnetic moment, in agreement with what is seen for the chemical analogs $YNiAl_4Ge_2$ and $LuNiAl_4Ge_2$ [5]. Evidence for antiferromagnetic-like ordering is seen upon further decreasing T, where $\chi_{dc}(T)$ for both field directions exhibits a maximum near $T_{N1} = 20.4$ K. For $H \parallel c$, this is followed by saturating behavior at low temperatures. In contrast, $\chi_{dc}(T)$ for $H \perp c$ exhibits a complex field and temperature dependence, as exemplified by the curves shown in Fig. 2(a) for $\mu_0 H = 0.5$ T. In particular, the zero-field-cooled (ZFC) curve initially shows a weak increase near 1.8–2.6 K, remains

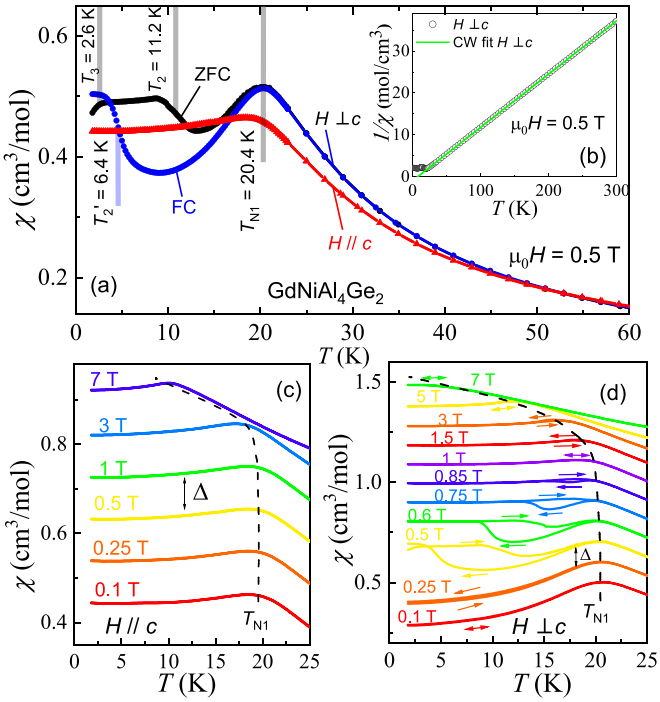

FIG. 2. (a) Temperature-dependent dc magnetic susceptibility $\chi_{dc}(T)$ for $GdNiAl_4Ge_2$ measured at $\mu_0 H = 0.5$ T applied parallel (∥) and perpendicular (⊥) to the crystalline c axis for temperatures $1.8\ \mathrm{K} \leqslant T \leqslant 60$ K. Both the zero-field-cooled (ZFC) and field-cooled (FC) scans are shown. Note that the feature at T_{N1} represents a thermodynamic phase transition while those at T_{N2} are not zero-field transitions, but rather represent the hysteretic field-driven transition between two different spin configurations (AFM1 and AFM2). (b) Inverse magnetic susceptibility $\chi^{-1}(T)$ for $\mu_0 H = 0.5$ T applied perpendicular to c. A Curie-Weiss (CW) fit to the data is shown as a solid green line. (c) $\chi(T)$ at various magnetic fields for $H \parallel c$ spanning the region where hysteresis is observed. (d) $\chi(T)$ at various magnetic fields for $H \perp c$. In (c) and (d), the data have been shifted vertically by constants Δ for clarity. The dashed curves are guides to the eye.

roughly constant up to 10 K, drops with an inflection point near 11.6 K, and then increases up to T_{N1}. In contrast, the field-cooled (FC) curve drops from its 1.8 K value through an inflection point near 6.4 K and then increases upon approaching T_{N1}. Over most of this temperature range, $\chi_{ZFC} > \chi_{FC}$. The features labeled T_{N2} represent the hysteretic field-driven transition between two different spin configurations [antiferromagnetic-like 1 and 2 (AFM1 and AFM2, respectively)], as evidenced by the spin-flop transitions that are seen in Fig. 3. The detailed field dependence of these features is shown in Fig. 2(d), where there is limited hysteresis for $\mu_0 H \leqslant 0.25$ T, strongly evolving hysteresis for $0.5 \leqslant \mu_0 H \leqslant 0.85$ T, and limited hysteresis for $\mu_0 H > 0.85$ T. For both field directions, we also find that increasing the magnetic field eventually suppresses T_{N1}. Finally, we note that in small fields these results resemble what was previously seen for polycrystalline specimens, although in that case $T_{N1} = 16.4$ K [5]. The reason for this difference is not obvious, but it might be attributed to chemical or structural variation that arises from the different synthesis methods.

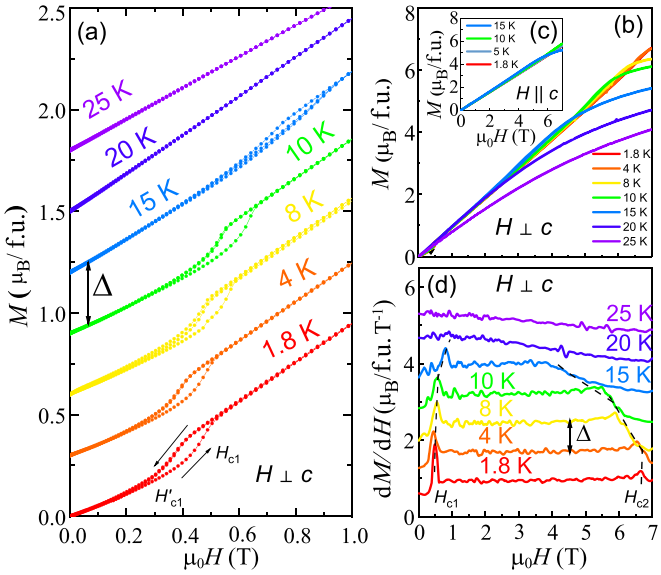

FIG. 3. (a) Isothermal magnetic-field-dependent magnetization $M(H)$ at various temperatures and magnetic fields $\mu_0 H \leqslant 1$ T for single-crystal $GdNiAl_4Ge_2$ with fields applied perpendicular (⊥) to the c axis. Curves are displaced by a constant Δ. (b) $M(H)$ for $H \perp c$ spanning 0–7 T. (c) $M(H)$ for $H \parallel c$. (d) The field derivative of the magnetization, $\partial M/\partial H$, for $H \perp c$. Data are shown for H-rising curves and are displaced by a constant Δ. The dashed curves track the peak positions of H_{c1} and H_{c2}. Here, f.u., formula unit.

The details of the magnetic order are further exposed by isothermal magnetization $M(H)$ curves (Fig. 3). At 1.8 K, $M_{\perp}(H)$ initially rises linearly, exhibits a small hysteretic region between $\mu_0 H_{c1} \approx 0.35$ T and $\mu_0 H_{c1} \approx 0.5$ T, and subsequently increases towards a limiting value near 6.7 μ_B/Gd atom near $\mu_0 H = 7$ T. This is 96% of the expected saturation value ($M_{sat} = g_J \mu_B J = 7\ \mu_B$/Gd atom for Gd^{3+}, where g_J is the Landé g-factor and J is the total angular momentum), showing that full saturation is likely to be reached without additional metamagnetic phase transitions. The low-field hysteretic region persists with increasing temperature, but it broadens and moves towards larger fields. At larger H, we also observe a shoulderlike feature at H_{c2} that moves towards lower fields with increasing temperature. In order to emphasize these details, the field derivative of the magnetization, $\partial M/\partial H$, is plotted in Fig. 3(d), where distinct boundaries are seen at H_{c1} and H_{c2}. As expected, $M(H)$ within the paramagnetic state ($T > T_{N1}$) is described by a Brillouin function that includes the ferromagnetic exchange interaction ($\theta = 6.2$ K), consistent with results from Curie-Weiss fits to $\chi(T)$ (Fig. S2 [44]). Finally, $M(H)$ for $H \parallel c$ shows no evidence for hysteresis, but the high-field boundary at H_{c2} is observed [Fig. 3(c)].

B. The ac magnetic susceptibility

Additional insight into the low-temperature magnetism is provided by the ac magnetic susceptibility $\chi'_{ac}(T)$, which was measured using a 1 mT oscillating field at several dc fields applied perpendicular to the c axis [Fig. 4(a)] and at frequencies ranging from 1 to 500 Hz [Fig. 4(b)]. Complex trends

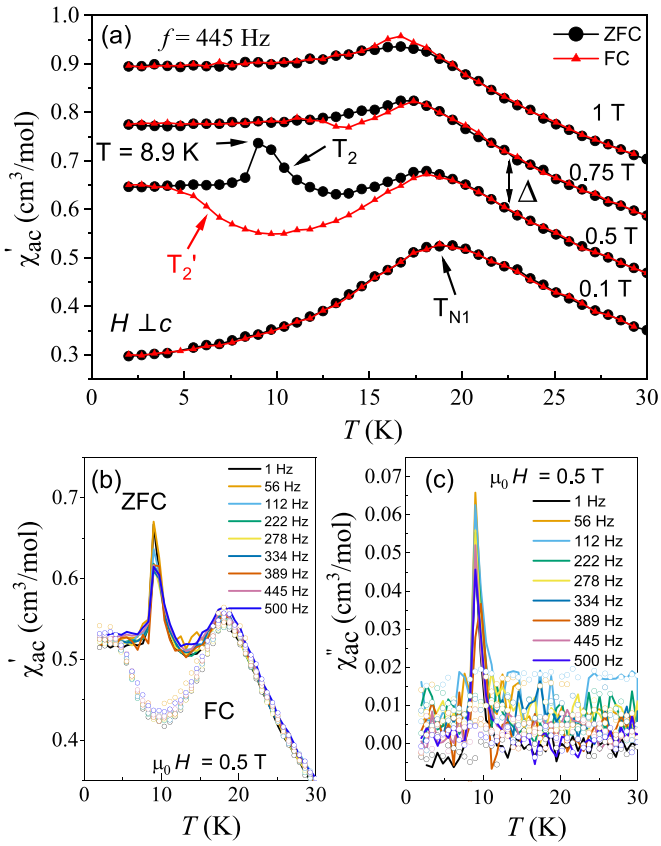

FIG. 4. (a) Temperature-dependent ac magnetic susceptibility $\chi'_{ac}(T)$ for magnetic fields H applied perpendicular ($\perp$) to the c axis. Both zero-field-cooled (ZFC) and field-cooled (FC) curves are shown. Curves are offset by a constant Δ. The features at T_{N1} and T_{N2} are described in the text. (b) $\chi'_{ac}(T)$ for $\mu_0 H = 0.5$ T applied perpendicular to c at several different excitation frequencies. Solid curves represent ZFC curves, and open circles represent FC curves. (c) $\chi''_{ac}(T)$ for $\mu_0 H = 0.5$ T applied perpendicular to c at several different excitation frequencies. Solid curves represent ZFC curves, and open circles represent FC curves.

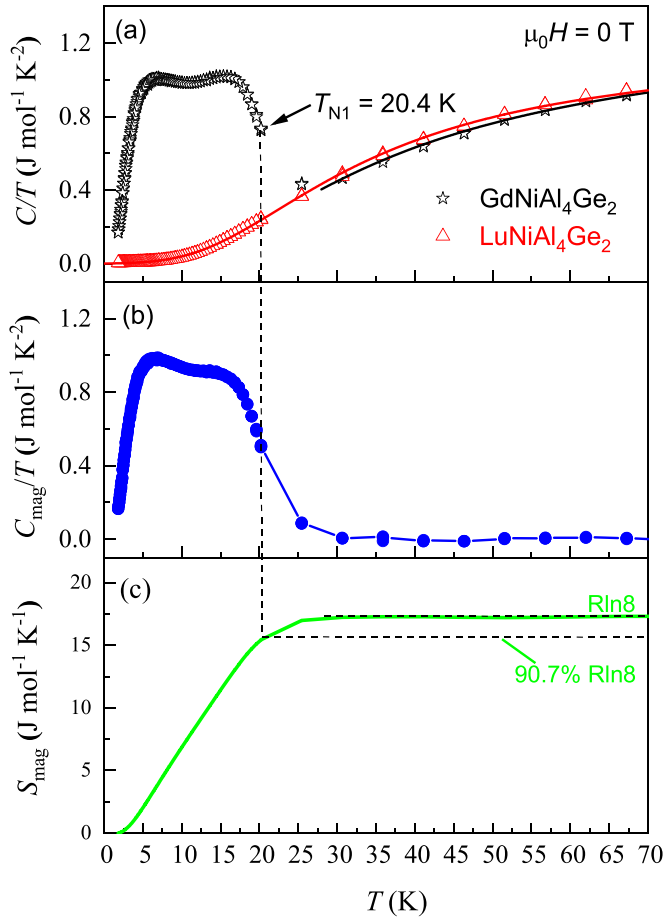

FIG. 5. (a) Heat capacity divided by temperature, C/T, vs T for single-crystal $GdNiAl_4Ge_2$ and $LuNiAl_4Ge_2$. The solid curves represent the fits that are described in the text. The antiferromagnetic ordering temperature at T_{N1} is indicated. (b) Magnetic specific heat divided by temperature, C_{mag}/T, vs T plotted for $GdNiAl_4Ge_2$. (c) Magnetic entropy S_{mag} vs T, which is obtained from the heat capacity data as described in the text.

are observed, mirroring results for $\chi_{dc}(T)$. Most notably, at $\mu_0 H = 0.5$ T the ZFC curve exhibits strong peaks in $\chi'_{ac}(T)$ and its derivative $\chi''_{ac}(T)$, whose amplitudes decrease with increasing frequency. In contrast, there is no peak for the FC curves, which closely resembles what is seen in the dc measurements. This implies that over the hysteresis region, the ZFC state hosts a distinct spin configuration that is characterized by frequency-dependent excitations with dynamic relaxation. Related results were seen for $Fe_{0.7}Co_{0.3}Si$, which exhibits a well-established skyrmion phase [47,48]. As revealed by the curve at 0.75 T, this behavior is not present over the entire hysteresis region, and large applied dc fields fully suppress it, likely as a result of spin polarization.

C. Heat capacity

The heat capacity divided by temperature, C/T, for $GdNiAl_4Ge_2$ and the corresponding nonmagnetic analog $LuNiAl_4Ge_2$ is shown in Fig. 5. As expected, there is close agreement between these curves at elevated temperatures, where phonons are the dominant term. Fits to the data are performed using the expression $C = \gamma T + C_{Debye}$, where γT is the electronic contribution and C_{Debye} is the integral Debye function. From this, we find Sommerfeld coefficients $\gamma_{Gd} = 2.2$ mJ/(mol K^2) and $\gamma_{Lu} = 1.3$ mJ/(mol K^2) and Debye temperatures $\theta_{Gd} = 141.4$ K and $\theta_{Lu} = 141.7$ K. The γ values are consistent with what is seen for other Gd-based intermetallics that have Fermi liquid ground states [49] and the similar values for θ_{Gd} and θ_{Lu} show that there is little impact on the phonon modes due to the differing molar masses between Gd and Lu. The impact of magnetic ordering is seen below 30 K, where there is evidence for a second-order phase transition at $T_{N1} = 20.4$ K, which is followed by a broad feature spanning low temperatures. In order to isolate the magnetic contribution C_{mag}/T, we subtract the electronic term and the integral Debye fit from the data, yielding the curve in Fig. 5(b). This reveals that magnetic fluctuations extend no higher than 30 K. From this, we calculate the magnetic entropy S_{mag} [Fig. 5(c)], where we find that 90.7% of $R\ln 8$ (where $R = 8.315$ J/(K mol) is the universal gas constant) is recovered at T_{N1} and 100% of $R\ln 8$ is recovered by 30 K, representing the full entropy of the $J = 7/2$ Gd^{3+} multiplet.

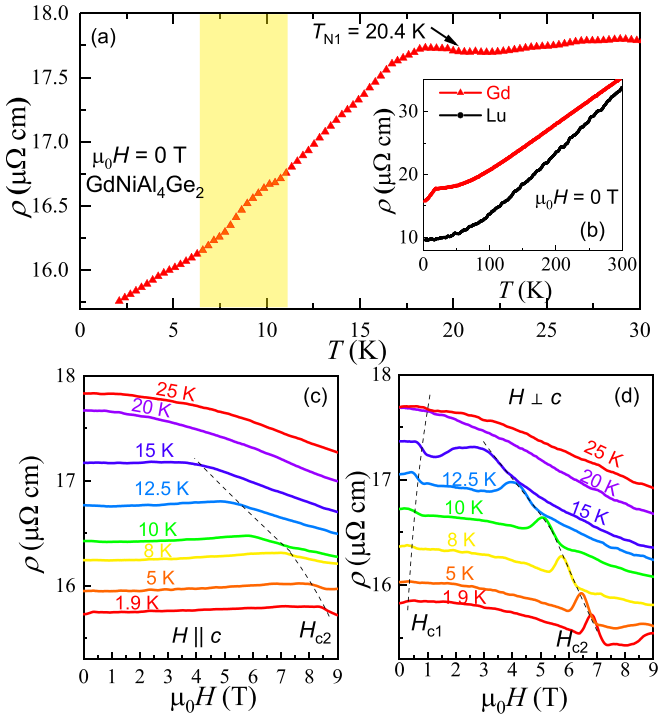

FIG. 6. (a) Temperature-dependent electrical resistivity $\rho(T)$ near the ordered state for $GdNiAl_4Ge_2$ measured at $\mu_0H = 0$ T. The antiferromagnetic phase transition at T_{N1} from $\chi(T)$ and $C(T)$ is indicated. (b) $\rho(T)$ for $GdNiAl_4Ge_2$ and $LuNiAl_4Ge_2$ for $T = 1.8$–300 K at $\mu_0H = 0$ T. (c) Field-dependent resistivity $\rho(H)$ for $GdNiAl_4Ge_2$ for electrical current I applied in the ab plane and magnetic field H applied parallel ($\parallel$) to the c axis. The dashed curve tracks the H_{c2} positions. (d) $\rho(H)$ for H applied perpendicular ($\perp$) to the c axis, where dashed curves track the peak positions of H_{c1} and H_{c2}.

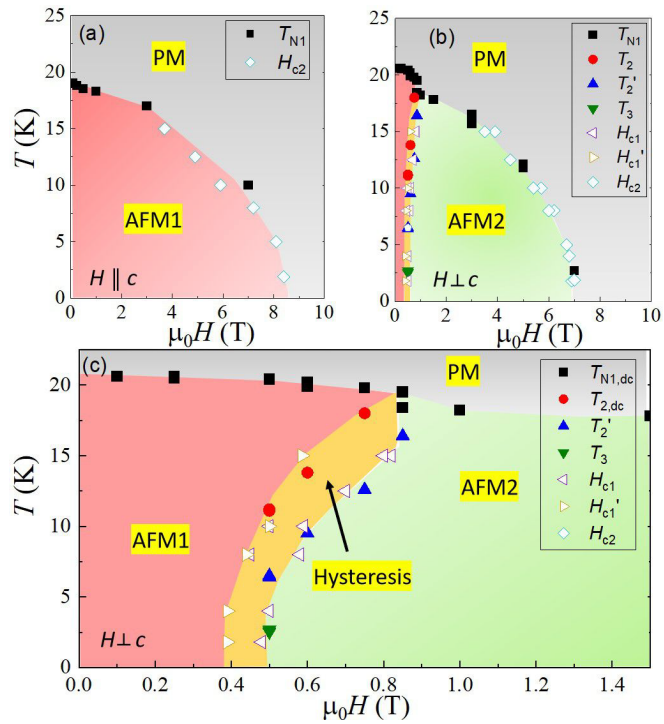

FIG. 7. Temperature T vs magnetic field μ_0H phase diagram for $GdAuAl_4Ge_2$ constructed from the magnetic susceptibility $\chi(T)$, isothermal magnetization $M(H)$, and electrical resistivity $\rho(T, H)$ measurements. The various paramagnetic (PM), antiferromagnetic (AFM), and hysteretic regions are described in the text. (a) T-H phase diagram for $H \parallel c$. (b) T-H phase diagram for $H \parallel ab$. (c) T-H phase diagram for $H \parallel ab$ shown over a limited field range in order to emphasize the low-field hysteresis region.

D. Electrical transport

The temperature-dependent electrical resistivities $\rho(T)$ for $GdNiAl_4Ge_2$ and $LuNiAl_4Ge_2$ are shown in Fig. 6. Both systems exhibit metallic behavior, where $\rho(T)$ decreases with decreasing T. At low temperatures, the magnetic ordering is seen as a reduction in $\rho(T)$ near T_{N1} due to the removal of spin disorder scattering. This is followed by a weak feature spanning the highlighted region in Fig. 6, indicating that there are additional spin fluctuations that scatter conduction electrons over this T range. The magnetoresistance $\rho(H)$ is shown in Figs. 6(c) and 6(d) for electrical current I applied in the ab plane and H applied parallel and perpendicular to the c axis. For $H \parallel c$, $\rho(H)$ weakly increases with positive curvature at 1.9 K and exhibits a kink near H_{c2}. This behavior persists with increasing T, where the kink moves towards lower fields and tracks the behavior seen in $\chi(T)$. More complex behavior is seen for $H \perp c$, where $\rho(H)$ initially decreases quadratically with increasing H at 1.9 K and then exhibits a pronounced peak at H_{c2}. This behavior is preserved up to T_{N1}, where the peak position gradually moves to lower H. An additional low-field feature is seen for $H \perp c$, which originates as a weak inflection point near H_{c1} but develops into a plateau with increasing T. This corresponds to the spin-flop transition that is observed in the magnetization measurements. Finally, all of these features disappear in the paramagnetic state, where $\rho(H)$ decreases quadratically with increasing H.

IV. DISCUSSION

These results are used to construct the T-H phase diagram shown in Fig. 7, where antiferromagnetic-like ordering (AFM1) initially emerges near $T_{N1} = 20.4$ K. For $H \parallel c$, T_{N1} is suppressed continuously with increasing field until it collapses to zero temperature near 8 T, consistent with what is seen for other antiferromagnetic systems where an applied field leads to the gradual coalignment of spins. Substantially more complex behavior is seen for $H \perp c$, where antiferromagnetic-like (AFM1) behavior occurs for small fields, but between 0.25 and 0.85 T, there is a T-dependent and hysteretic spin-flop transition into a region labeled AFM2. This not only impacts the dc magnetic response, but also is observed as a plateau in the magnetoresistance. For a limited portion of the hysteresis region, there are also frequency-dependent peaks in both χ'_{ac} and χ''_{ac}. This indicates that this region harbors fragile spin structures that not only scatter electrons, but also exhibit dynamic history-dependent relaxation. It is also noteworthy that the temperature range for the hysteresis coincides with a broad hump that is seen in C/T and other features in $\rho(T)$, suggesting that even the zero-field state includes nascent magnetic complexity. Finally, for larger

H, the antiferromagnetic order (AFM2) is suppressed and collapses towards $T = 0$ K near 7 T.

In many ways, this behavior resembles what is seen for a classic spin-flop transition [25–27]. However, given the combination of the geometrically frustrated crystalline lattice and the potentially complex RKKY interaction, it is of interest to make comparisons with related systems with unusual behavior. For example, it has already been shown that there is a diversity of helical spin states in Gd-based intermetallics with centrosymmetric crystalline structures [15,23,24]. This is highlighted by Gd_2PdSi_3, which includes planar triangular Gd nets and unexpectedly exhibits both helical order and skyrmion states. Amongst 1142 compounds, the chemical analog $GdAuAl_4Ge_2$ exhibits antiferromagnetic-like phase transitions at $T_{N1} = 17.8$ K, $T_{N2} = 15.6$ K, and $T_{N2} = 13.8$ K [2], each of which represents a distinct thermodynamic ordered state. For $H \parallel c$, these transitions are suppressed with increasing field and are extrapolated to approach $T = 0$ near $\mu_0 H = 10$ T. In contrast, for fields applied perpendicular to c, there are a series of metamagnetic phase transitions that lead to the emergence of several additional distinct ordered states. This suggests that $GdAuAl_4Ge_2$ and $GdNiAl_4Ge_2$ are described by related scenarios, where the balance of competing interactions allows for the formation of distinct thermodynamic phases for the former case, and instead leads to a region of complex and hysteretic spin structures in the latter.

We additionally remark that evidence for magnetic frustration is provided by (i) the contrast between the antiferromagnetic-like ordering and the positive value of θ (which indicates a ferromagnetic spin exchange) and (ii) the observation that $\theta < T_{N1}$, which implies that there are competing ferromagnetic and antiferromagnetic spin exchange parameters [50]. It is natural to associate this behavior with the triangular nets [8,15,50], but such behavior also could result from the Ruderman-Kittel-Kasuya-Yosida (RKKY) interaction, where the conduction electrons provide a long-range spin exchange mechanism that is governed by the Fermi surface topography [51–53]. This can lead to complex phase diagrams, e.g., as seen for the anisotropic next-nearest-neighbor Ising (ANNNI) model [54], where competition between nearest- and next-nearest-neighbor spin exchange interactions produces ordered states with a wave vector Q that is sensitive to external parameters such as temperature and field. Alternatively, it was recently proposed that the formation of helical magnetic structures in some centrosymmetric Gd-based materials is related to interorbital frustration between Gd $5d$ and $4f$ orbitals [18]. Finally, it is conceivable that there are simple spin alignments within planes, but with complex intraplane modulation. Additional measurements, such as measurements of neutron scattering or nuclear magnetic resonance, are needed to clarify these possibilities.

V. CONCLUSIONS

We have uncovered rich phenomena in $GdNiAl_4Ge_2$, which exhibits local $4f$ moment magnetic ordering at $T_{N1} = 20.4$ K. Complex behavior emerges when magnetic fields are applied in the triangular net plane of the Gd atoms, where (i) antiferromagnetic-like behavior occurs for small fields, (ii) a spin-flop transition and magnetic hysteresis are seen for $\mu_0 H = 0.5$–0.85 T, and (iii) the antiferromagnetic order is gradually suppressed and collapses towards $T = 0$ K near 7 T. Together with the frequency- and history-dependent ac magnetic susceptibility and magnetoresistance measurements, this implies the formation of history-dependent spin structures or domains with complex spin relaxation dynamics. While spin-flop behavior is well known, the hysteresis region may host novel phenomena that resemble what is seen in other materials with nontrivial spin textures. This invites further measurements to quantify the microscopic details of the ordered states (e.g., using neutron scattering, Lorentz tunneling electron microscopy, or magnetic force microscopy), the spin relaxation dynamics, and the impact on the electronic, magnetic, and structural properties (e.g., angle-resolved photoemission spectroscopy, Hall effect, and magnetostriction) for $GdNiAl_4Ge_2$ and its chemical relatives.

ACKNOWLEDGMENTS

R.B. and K.F. were supported by the National Science Foundation through NSF Grant No. DMR-1904361. The National High Magnetic Field Laboratory is supported by the National Science Foundation through NSF Grant No. DMR-1644779 and the State of Florida. We are grateful for productive conversations with Andrew Christianson at Oak Ridge National Laboratory.

[1] K. Feng, I. A. Leahy, O. Oladehin, K. Wei, M. Lee, and R. Baumbach, Magnetic ordering in $GdAuAl_4Ge_2$ and $TbAuAl_4Ge_2$: Layered compounds with triangular lanthanide nets, J. Magn. Magn. Mater. **564**, 170006 (2022).

[2] I. A. Leahy, K. Feng, R. Dery, R. Baumbach, and M. Lee, Field-induced magnetic states in the metallic rare-earth layered triangular antiferromagnet $TbAuAl_4Ge_2$, Phys. Rev. B **106**, 094426 (2022).

[3] M. Cong, H. Ge, L. Zhang, W. Ren, N. Zhao, T. Li, S. Wang, J. Zhu, J. Mei, Q. Zhang, J. Sheng, F. Gao, B. Li, Z. Zhang, and L. Wu, Magnetic phase diagram and multiple field-induced states in the intermetallic triangular-lattice antiferromagnet $NdAuAl_4Ge_2$ with Ising-like spins, Phys. Rev. Mater. **7**, 024423 (2023).

[4] K. Feng, C. Bush, O. Oladehin, M. Lee, and R. Baumbach, Complex antiferromagnetic order in the metallic triangular lattice compound $SmAuAl_4Ge_2$, arXiv:2308.13945.

[5] M. Witt, J. Bönnighausen, F. Eustermann, A. Savourat, J. P. Scheifers, B. P. T. Fokwa, C. Doerenkamp, H. Eckert, and O. Janka, Extending the knowledge on the quaternary rare earth nickel aluminum germanides of the $RENiAl_4Ge_2$ series (RE = Y, Sm, Gd–Tm, Lu)−structural, magnetic and NMR-spectroscopic investigations, Z. Naturforsch. B **75**, 149 (2020).

[6] C. Zhang, Y. Wang, F. Zhang, H. R. Y. Cai, L. Wang, X.-M. Ma, S. Guo, Z. Chen, Y. Wang, Z. Jiang, Y. Yang, Z. Liu, M. Ye, J. Lin, J. Mei, Z. Hao, Z. Xie, and C. Chen, Multiple surface states, nontrivial band topology and antiferromagnetism in $GdAuAl_4Ge_2$, Chin. Phys. B **32**, 077401 (2023).

[7] T. T. A. Lummen, I. P. Handayani, M. C. Donker, D. Fausti, G. Dhalenne, P. Berthet, A. Revcolevschi, and P. H. M. van Loosdrecht, Phonon and crystal field excitations in geometrically frustrated rare earth titanates, Phys. Rev. B **77**, 214310 (2008).

[8] S. Pakhira, C. Mazumdar, R. Ranganathan, S. Giri, and M. Avdeev, Large magnetic cooling power involving frustrated antiferromagnetic spin-glass state in R_2NiSi_3(R = Gd, Er), Phys. Rev. B **94**, 104414 (2016).

[9] E. A. Goremychkin, R. Osborn, B. D. Rainford, R. T. Macaluso, D. T. Adroja, and M. Koza, Spin-glass order induced by dynamic frustration, Nat. Phys. **4**, 766 (2008).

[10] B. R. Ortiz, L. C. Gomes, J. R. Morey, M. Winiarski, M. Bordelon, J. S. Mangum, I. W. H. Oswald, J. A. Rodriguez-Rivera, J. R. Neilson, S. D. Wilson, E. Ertekin, T. M. McQueen, and E. S. Toberer, New kagome prototype materials: Discovery of KV_3Sb_5, RbV_3Sb_5, and CsV_3Sb_5, Phys. Rev. Mater. **3**, 094407 (2019).

[11] B. R. Ortiz, S. M. L. Teicher, Y. Hu, J. L. Zuo, P. M. Sarte, E. C. Schueller, A. M. M. Abeykoon, M. J. Krogstad, S. Rosenkranz, R. Osborn, R. Seshadri, L. Balents, J. He, and S. D. Wilson, CsV_3Sb_5: A $\mathbb{Z}_2$ topological kagome metal with a superconducting ground state, Phys. Rev. Lett. **125**, 247002 (2020).

[12] M. Ezawa, Higher-order topological insulators and semimetals on the breathing kagome and pyrochlore lattices, Phys. Rev. Lett. **120**, 026801 (2018).

[13] M. Kang, S. Fang, L. Ye, H. C. Po, J. Denlinger, C. Jozwiak, A. Bostwick, E. Rotenberg, E. Kaxiras, J. G. Checkelsky, and R. Comin, Topological flat bands in frustrated kagome lattice CoSn, Nat. Commun. **11**, 4004 (2020).

[14] B. C. Sales, W. R. Meier, A. F. May, J. Xing, J.-Q. Yan, S. Gao, Y. H. Liu, M. B. Stone, A. D. Christianson, Q. Zhang, and M. A. McGuire, Tuning the flat bands of the kagome metal CoSn with Fe, In, or Ni doping, Phys. Rev. Mater. **5**, 044202 (2021).

[15] T. Kurumaji, T. Nakajima, M. Hirschberger, A. Kikkawa, Y. Yamasaki, H. Sagayama, H. Nakao, Y. Taguchi, T. H. Arima, and Y. Tokura, Skyrmion lattice with a giant topological Hall effect in a frustrated triangular-lattice magnet, Science **365**, 914 (2019).

[16] Q. Wang, S. Sun, X. Zhang, F. Pang, and H. Lei, Anomalous Hall effect in a ferromagnetic Fe_3Sn_2 single crystal with a geometrically frustrated Fe bilayer kagome lattice, Phys. Rev. B **94**, 075135 (2016).

[17] Q. Wang, K. J. Neubauer, C. Duan, Q. Yin, S. Fujitsu, H. Hosono, F. Ye, R. Zhang, S. Chi, K. Krycka, and H. Lei, Field-induced topological Hall effect and double-fan spin structure with a c-axis component in the metallic kagome antiferromagnetic compound YMn_6Sn_6, Phys. Rev. B **103**, 014416 (2021).

[18] T. Nomoto, T. Koretsune, and R. Arita, Formation mechanism of the helical Q structure in Gd-based skyrmion materials, Phys. Rev. Lett. **125**, 117204 (2020).

[19] Y. Zhang, J. Liu, Y. Dong, S. Wu, J. Zhang, J. Wang, J. Lu, A. Rückriegel, H. Wang, R. Duine, H. Yu, Z. Luo, K. Shen, and J. Zhang, Strain-driven Dzyaloshinskii-Moriya interaction for room-temperature magnetic skyrmions, Phys. Rev. Lett. **127**, 117204 (2021).

[20] S. Gao, H. D. Rosales, F. A. Gómez Albarracín, V. Tsurkan, G. Kaur, T. Fennell, P. Steffens, M. Boehm, P. Čermák, A. Schneidewind, E. Ressouche, D. C. Cabra, C. Rüegg, and O. Zaharko, Fractional antiferromagnetic skyrmion lattice induced by anisotropic couplings, Nature (London) **586**, 37 (2020).

[21] S. Hayami, Multifarious skyrmion phases on a trilayer triangular lattice, Phys. Rev. B **105**, 184426 (2022).

[22] Z. Hou, L. Li, C. Liu, X. Gao, Z. Ma, G. Zhou, Y. Peng, M. Yan, X.-X. Zhang, and J. Liu, Emergence of room temperature stable skyrmionic bubbles in the rare earth based $REMn_2Ge_2$ (RE = Ce, Pr, and Nd) magnets, Mater. Today Phys. **17**, 100341 (2021).

[23] M. Hirschberger, T. Nakajima, S. Gao, L. Peng, A. Kikkawa, T. Kurumaji, M. Kriener, Y. Yamasaki, H. Sagayama, H. Nakao, K. Ohishi, K. Kakurai, Y. Taguchi, X. Yu, T.-h. Arima, and Y. Tokura, Skyrmion phase and competing magnetic orders on a breathing kagomé lattice, Nat. Commun. **10**, 5831 (2019).

[24] N. D. Khanh, T. Nakajima, X. Z. Yu, S. Gao, K. Shibata, M. Hirschberger, Y. Yamasaki, H. Sagayama, H. Nakao, L. C. Peng, K. Nakajima, R. Takagi, T. Arima, Y. Tokura, and S. Seki, Nanometric square skyrmion lattice in a centrosymmetric tetragonal magnet, Nat. Nanotechnol. **15**, 444 (2020).

[25] S. Foner, Antiferromagnetic and ferrimagnetic resonance, in *Magnetism*, edited by G. T. Rado and H. Suhl (Academic, New York, 1963), Vol. I, Chap. 9, p. 384.

[26] L. J. De Jongh and A. R. Miedema, Experiments on simple magnetic model systems, Adv. Phys. **50**, 947 (2001).

[27] T. Nagamiya, K. Yosida, and R. Kubo, Antiferromagnetism, Adv. Phys. **4**, 1 (1955).

[28] S. Mühlbauer, B. Binz, F. Jonietz, C. Pfleiderer, A. Rosch, A. Neubauer, R. Georgii, and P. Böni, Skyrmion lattice in a chiral magnet, Science **323**, 915 (2009).

[29] Y. Ishikawa and M. Arai, Magnetic phase diagram of MnSi near critical temperature studied by neutron small angle scattering, J. Phys. Soc. Jpn. **53**, 2726 (1984).

[30] C. Pfleiderer, D. Reznik, L. Pintschovius, H. v. Löhneysen, M. Garst, and A. Rosch, Partial order in the non-Fermi-liquid phase of MnSi, Nature (London) **427**, 227 (2004).

[31] M. Janoschek, M. Garst, A. Bauer, P. Krautscheid, R. Georgii, P. Böni, and C. Pfleiderer, Fluctuation-induced first-order phase transition in Dzyaloshinskii-Moriya helimagnets, Phys. Rev. B **87**, 134407 (2013).

[32] B. Lebech, J. Bernhard, and T. Freltoft, Magnetic-structures of cubic FeGe studied by small-angle neutron scattering, J. Phys.: Condens. Matter **1**, 6105 (1989).

[33] X. Z. Yu, N. Kanazawa, Y. Onose, K. Kimoto, W. Z. Zhang, S. Ishiwata, Y. Matsui, and Y. Tokura, Near room-temperature formation of a skyrmion crystal in thin-films of the helimagnet FeGe, Nat. Mater. **10**, 106 (2011).

[34] H. Wilhelm, M. Baenitz, M. Schmidt, U. K. Rößler, A. A. Leonov, and A. N. Bogdanov, Precursor phenomena at the magnetic ordering of the cubic helimagnet FeGe, Phys. Rev. Lett. **107**, 127203 (2011).

[35] T. Adams, A. Chacon, M. Wagner, A. Bauer, G. Brandl, B. Pedersen, H. Berger, P. Lemmens, and C. Pfleiderer, Long-wavelength helimagnetic order and skyrmion lattice phase in Cu_2OSeO_3, Phys. Rev. Lett. **108**, 237204 (2012).

[36] O. Janson, I. Rousochatzakis, A. A. Tsirlin, M. Belesi, A. A. Leonov, U. K. Rößler, J. van den Brink, and H. Rosner, The quantum nature of skyrmions and half-skyrmions in Cu_2OSeO_3, Nat. Commun. **5**, 5376 (2014).

[37] W. Münzer, A. Neubauer, T. Adams, S. Mühlbauer, C. Franz, F. Jonietz, R. Georgii, P. Böni, B. Pedersen, M. Schmidt, A. Rosch, and C. Pfleiderer, Skyrmion lattice in the doped semiconductor $Fe_{1-x}Co_xSi$, Phys. Rev. B **81**, 041203(R) (2010).

[38] C. Pfleiderer, T. Adams, A. Bauer, W. Biberacher, B. Binz, F. Birkelbach, P. Böni, C. Franz, R. Georgii, M. Janoschek, F. Jonietz, T. Keller, R. Ritz, S. Mühlbauer, W. Münzer, A. Neubauer, B. Pedersen, and A. Rosch, Skyrmion lattices in metallic and semiconducting B20 transition metal compounds, J. Phys.: Condens. Matter **22**, 164207 (2010).

[39] C. Zhang, C. Liu, J. Zhang, Y. Yuan, Y. Wen, Y. Li, D. Zheng, Q. Zhang, Z. Hou, G. Yin, K. Liu, Y. Peng, and X.-X. Zhang, Room-temperature magnetic skyrmions and large topological Hall effect in chromium telluride engineered by self-intercalation, Adv. Mater. **35**, 2205967 (2023).

[40] X. Tan, M. Berg, A. de Lozanne, J. Kim, R. E. Baumbach, E. D. Bauer, J. D. Thompson, and F. Ronning, Imaging the magnetic states in an actinide ferromagnet UMn_2Ge_2, Phys. Rev. Mater. **2**, 074402 (2018).

[41] D. Wulferding, H. Kim, I. Yang, J. Jeong, K. Barros, Y. Kato, I. Martin, O. E. Ayala-Valenzuela, M. Lee, H. C. Choi, F. Ronning, L. Civale, R. E. Baumbach, E. D. Bauer, J. D. Thompson, R. Movshovich, and J. Kim, Domain engineering of the metastable domains in the 4f-uniaxial-ferromagnet $CeRu_2Ga_2B$, Sci. Rep. **7**, 46296 (2017).

[42] L. Balents, Spin liquids in frustrated magnets, Nature (London) **464**, 199 (2010).

[43] P. C. Canfield, T. Kong, U. S. Kaluarachchi, and N. H. Jo, Use of frit-disc crucibles for routine and exploratory solution growth of single crystalline samples, Philos. Mag. **96**, 84 (2016).

[44] See Supplemental Material at http://link.aps.org/supplemental/10.1103/PhysRevMaterials.7.124409 for the Rietveld refinements of powder x-ray diffraction patterns of $LuNiAl_4Ge_2$ and a comparison between (i) the magnetization vs. magnetic field $M(H)$ at $T = 25$ K (i.e., within the paramagnetic state) for H applied in the *ab* plane for $GdNiAl_4Ge_2$ and (ii) an ideal magnetization curve.

[45] K. Momma and F. Izumi, *VESTA 3* for three-dimensional visualization of crystal, volumetric and morphology data, J. Appl. Crystallogr. **44**, 1272 (2011).

[46] S. Legvold, Rare earth metals and alloys, in *Ferromagnetic Materials: A Handbook on the Properties of Magnetically Ordered Substances*, Handbook of Ferromagnetic Materials Vol. 1 (Elsevier, New York, 1980), Chap. 3, pp. 183–295.

[47] T. Y. Ou-Yang, G. J. Shu, C. D. Hu, and F. C. Chou, Dynamic susceptibility study on the skyrmion phase stability of $Fe_{0.7}Co_{0.3}Si$, J. Appl. Phys. **117**, 123903 (2015).

[48] L. J. Bannenberg, A. J. E. Lefering, K. Kakurai, Y. Onose, Y. Endoh, Y. Tokura, and C. Pappas, Magnetic relaxation phenomena in the chiral magnet $Fe_{1-x}Co_xSi$: An ac susceptibility study, Phys. Rev. B **94**, 134433 (2016).

[49] M. Bouvier, P. Lethuillier, and D. Schmitt, Specific heat in some gadolinium compounds. I. Experimental, Phys. Rev. B **43**, 13137 (1991).

[50] A. P. Ramirez, Strongly geometrically frustrated magnets, Annu. Rev. Mater. Sci. **24**, 453 (1994).

[51] M. A. Ruderman and C. Kittel, Indirect exchange coupling of nuclear magnetic moments by conduction electrons, Phys. Rev. **96**, 99 (1954).

[52] K. Yosida, Magnetic properties of Cu-Mn alloys, Phys. Rev. **106**, 893 (1957).

[53] T. Kasuya, A theory of metallic ferro- and antiferromagnetism on Zener's model, Prog. Theor. Phys. **16**, 45 (1956).

[54] W. Selke, The ANNNI model–Theoretical analysis and experimental application, Phys. Rep. **170**, 213 (1988).